ADVANCED QUANTUM TECHNOLOGIES
www.advquantumtech.com

# Heteroepitaxial (111) Diamond Quantum Sensors with Preferentially Aligned Nitrogen-Vacancy Centers for an Electric Vehicle Battery Monitor

*Kenichi Kajiyama, Moriyoshi Haruyama, Yuji Hatano, Hiromitsu Kato, Masahiko Ogura, Toshiharu Makino, Hitoshi Noguchi, Takeharu Sekiguchi, Takayuki Iwasaki, and Mutsuko Hatano**

**A platform for heteroepitaxial (111) chemical vapor deposition (CVD) diamond quantum sensors with preferentially aligned nitrogen vacancy (NV) centers on a large substrate is developed, and its operation as an electric vehicle (EV) battery monitor is demonstrated. A self-standing heteroepitaxial CVD diamond film with a (111) orientation and a thickness of 150 µm is grown on a non-diamond substrate and subsequently separated from it. The high uniformity and crystallinity of the (111)-oriented diamond is confirmed. A 150-µm thick NV-diamond layer is then deposited on the heteroepitaxial diamond. The $T_2$ value measured by confocal microscopy is 20 µs, which corresponds to substitutional nitrogen defect concentration of 8 ppm. The nitrogen-vacancy concentration and $T_2^*$ are estimated to be 0.05 ppm and 0.05 µs by continuous wave optically detected magnetic resonance (CW-ODMR) spectroscopy in a fiber-top sensor configuration. In a gradiometer, where two sensors are placed on both sides of the busbar, the noise floor is 17 nT/Hz$^{0.5}$ in the frequency range of 10–40 Hz without magnetic shielding. The Allan deviation of the magnetic field noise in the laboratory is below 0.3 µT, which corresponds to a busbar current of 10 mA, in the accumulation time range of 10 ms to 100 s.**

## 1. Introduction

Nitrogen vacancy (NV) centers in diamond have been shown to be one of the most specific localized electronic structures to serve as spin-based qubits and are promising candidates for quantum sensors.[1–5] The superior properties of wide dynamic range, high accuracy, and high sensitivity make the diamond quantum sensor suitable for high-precision measurement of battery currents in electric vehicles (EV). In a previous study, current monitoring without magnetic shielding with an accuracy of 10 mA and dynamic range of ±1000 A was demonstrated in the automotive operating temperature range of −40 to 85 °C using Ib-type diamond quantum sensors grown at High-Pressure and High-Temperature (HPHT).[6] The linearity and the current detectability under an external magnetic field noise of 80 µT, which is larger than that of 50 µT around the EV battery module in a real car during driving was confirmed.[7] The wide operating temperature range of −150 to 150 °C was also reported.[8] These performances are expected to improve the efficiency of EV batteries by 10% and contribute to the higher performance of EVs. To use diamond quantum sensors as EV battery monitors, their industrial productivity needs to be demonstrated at this stage.

Although HPHT diamonds or homoepitaxial chemical vapor deposition (CVD) diamonds grown on HPHT seed crystals are of high quality, there are issues concerning size and cost. Heteroepitaxial CVD[9–28] diamond on large substrates is a key technology in terms of scalability and productivity of the diamond quantum sensors. Heteroepitaxial CVD diamonds with a diameter of several centimeters grown on Ir/YSZ/Si[20,21,27] or Ir/Sapphire[23,24,28] substrates have already been reported. From the application point of view, diamond sensors with NV or Silicon Vacancy (SiV) centers,[16,17,21] as well as power electronics[15,23,24,28] or thermal heatsinks,[22] have been studied. Furthermore, for highly sensitive quantum sensors, controlling the NV axis alignment is crucial, and CVD growth on the (111) single-crystal substrate leads to preferential alignment to the [111] direction.[29–33]

K. Kajiyama, Y. Hatano, T. Sekiguchi, T. Iwasaki, M. Hatano
Department of Electrical and Electronics Engineering
School of Engineering
Institute of Science Tokyo
2-12-1 NE18, Oolayama, Meguro-ku, Tokyo 152-8552, Japan
E-mail: hatano.m.ab@m.titech.ac.jp

M. Haruyama, H. Kato, M. Ogura, T. Makino
Advanced Power Electronics Research Center
National Institute of Advanced Industrial Science and Technology (AIST)
1-1-1, Umezono, Tsukuba, Ibaraki 305–8568, Japan

H. Noguchi
Advanced Functional Materials Research Center
Shin-Etsu Chemical Co., Ltd
2-13-1, Isobe, Annaka, Gunma 379-0195, Japan

The ORCID identification number(s) for the author(s) of this article can be found under https://doi.org/10.1002/qute.202400400



**DOI: 10.1002/qute.202400400**

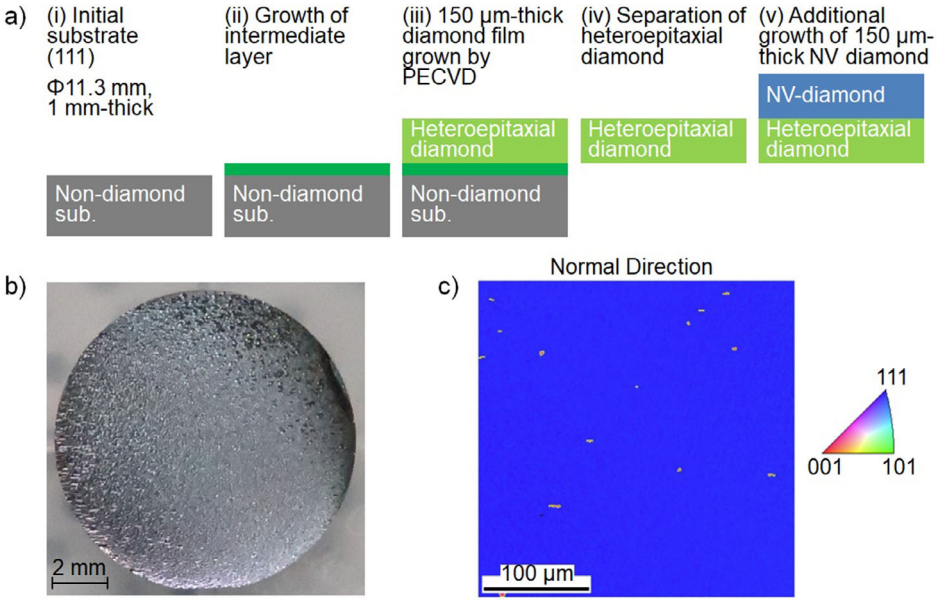


**Figure 1.** Heteroepitaxial (111) CVD diamond process with preferentially aligned NV centers. a) Process flow. b) Top-view of heteroepitaxial diamond (iii). c) Inverse pole figure map of heteroepitaxial diamond (iii).

Here, a platform for heteroepitaxial (111) diamond quantum sensors with preferentially aligned NV centers on large substrates has been developed that could facilitate their implementation as EV battery monitors. A 150 μm thick self-standing heteroepitaxial CVD diamond substrate grown on a (111) non-diamond substrate was formed and high uniformity and crystallinity of the (111)-oriented diamonds were confirmed. Subsequently, a diamond with a diameter of 11.3 mm was cut into 2 mm squares and then a 150 μm thick NV-contained diamond layer with preferentially aligned NV axis was deposited on the heteroepitaxial CVD diamond. Owing to the processing steps mentioned above, such as crystal growth, polishing, and shaping, the orientation of the NV axis is not always perpendicular to the substrate surface. Therefore, a tilt correction mechanism was incorporated into the sensor holder to enable the exact measurement of the [111]-direction magnetic field, even when the misorientation between the [111]-direction and the substrate normal was greater than 10°.

In this manuscript, the heteroepitaxial (111) CVD diamond process with preferentially aligned NV centers is presented first. Then, the structure of the EV battery monitor using the diamonds including the tilt correction mechanism is explained. After that, the results of confocal microscopy to evaluate the fundamental physical properties are explained. The fundamental performance of the diamonds as the fiber-top sensor installed in the sensor holder is also shown. Finally, the common mode noise rejection characteristics as the gradiometer in the laboratory noise environment are demonstrated. Furthermore, a perspective for ensuring the required noise immunity in the in-vehicle noise environment is discussed.

## 2. Fabrication Process

Heteroepitaxial CVD diamonds were synthesized on heterogeneous non-diamond substrates. A substrate larger than the homoepitaxial CVD diamond synthesized on HPHT diamond is possible and, therefore, superior in industrial productivity. By using (111) heterogeneous substrates, (111)-oriented surface, which is suitable for impurity doping and $NV^-$ axis control is realized as an intrinsic feature of CVD diamond.

**Figure 1a** shows the process flow for the heteroepitaxial diamond substrate. The starting material was a non-diamond substrate with a diameter of 11.3 mm and a thickness of 1 mm. After growing some intermediate layers, a non-doped diamond crystal with a thickness of 150 μm was heteroepitaxially grown by microwave plasma CVD. Figure 1b shows a top view of the heteroepitaxial diamond. The non-diamond substrate was then separated and cut to obtain a freestanding heteroepitaxial diamond substrate, as shown in Figure 1a(iv). The crystallinity of the heteroepitaxial diamond was evaluated by electron backscatter diffraction (EBSD), in which the distribution of the crystallographic surface orientation was determined by observing electron beam diffraction. Figure 1c shows a typical EBSD image of a heteroepitaxial diamond substrate. The observation area was 300 μm square at 1 μm resolution. Uniform mapping images with (111) orientation were obtained from the entire surface area, indicating the high uniformity and crystallinity of (111)-oriented diamond. Additional NV diamond layers with a thickness of 150 μm were grown on heteroepitaxial diamond substrates by microwave plasma CVD. A mixture of purified hydrogen, isotopically enriched $^{12}C$ methane, and nitrogen was used as the source gas. The typical CVD growth parameters were 120 Torr, 3500 W, $^{12}CH_4/H_2 = 0.1\%$, and $N_2/^{12}CH_4 = 5\%$ for 96 h.

In (111) heteroepitaxial diamond growth, the initial stage of crystal growth tends to show low orientation and many dislocation defects. Moreover, the crystal alignment may be disturbed during nitrogen-doped growth. Therefore, we decided to first form an undoped heteroepitaxial diamond (111) layer with sufficient crystal orientation, and then cover it with a nitrogen-doped diamond layer to create many NV centers.

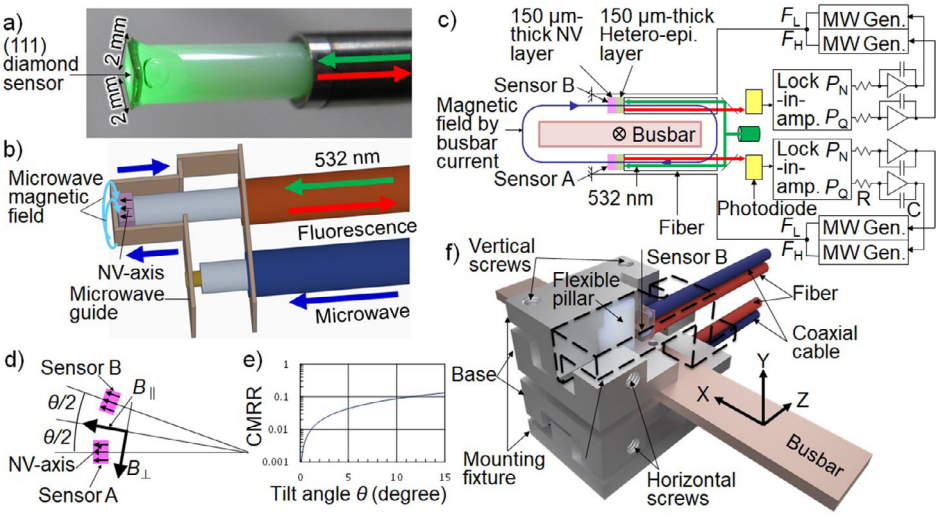


**Figure 2.** Electric vehicle (EV) battery monitor with heteroepitaxial (111) diamond sensors. a) Diamond sensor glued to the fiber top. b) Microwave guide surrounding the fiber top to generate a microwave magnetic field perpendicular to the [111] NV-axis of the diamond sensor. c) Circuit for tracking the resonance frequencies of two sensors A and B for the gradiometer. The higher and lower resonance frequencies of each sensor, $R_H$ and $R_L$, are tracked by two microwave generators' frequencies $F_H$ and $F_L$ at the same time using integral feedback control from the normal and quadrature two-phase outputs of the lock-in amplifier, $P_N$ and $P_Q$. d) Illustration of the tilt angle $\theta$ between two sensors A and B. e) Dependence of the CMRR (Common Mode Rejection Ratio) on $\theta$. f) Illustration of the tilt correction mechanism in the sensor holder. The sensor holder consists of the base and the mounting fixture. The base is attached to the bus bar. The base and the mounting fixture are connected by the flexible pillar. The sensor is fixed to the mounting fixture. The tilt angle between the sensor surface and the busbar was fine-tuned using these screws. The top half of the upper sensor holder is shown as a dashed outline line to clearly show the area around sensor B. Sensor A is located under the busbar and is not visible in this illustration.

## 3. EV Battery Monitor with Heteroepitaxial (111) Diamond Sensors

The structure of the EV battery monitor with heteroepitaxial (111) diamond sensors is shown in **Figure 2**. Figure 2a shows the diamond sensor glued to the top of the multimode optical fiber with a numerical aperture of 0.5 and a core diameter of 400 µm (FR400URT, Thorlabs). Figure 2b shows the microwave guide surrounding the sensor head and connected to the end of the coaxial cable. A microwave magnetic field was applied perpendicular to the [111] NV axis of the diamond.

Two sensors, A and B, were placed above and below the busbar to form the gradiometer, as shown in Figure 2c, so that the current magnetic field was obtained as the differential output of both sensors and the noise of the ambient magnetic field was eliminated as a common mode. The metallic busbar effectively blocked the microwave and fluorescence interference between the two sensors, which ensured the accuracy of differential detection.

To separate the effect of temperature fluctuation from the measured magnetic field, the higher and lower [111] resonance frequencies, $R_H$ and $R_L$, are tracked by two microwave generators' frequencies $F_H$ and $F_L$ at the same time using integral feedback control from the normal and quadrature two-phase outputs of the lock-in amplifier, $P_N$ and $P_Q$.[34] Since the integration time constant was CR = 0.1 s, $R_H$ and $R_L$ cannot be tracked exactly by $F_H$ and $F_L$, and the real magnetic field $(R_H - R_L)/2\gamma$ could differ from the measurable value of $(F_H - F_L)/2\gamma$ if they change faster than 0.1 s, where $\gamma$ is the gyromagnetic ratio. However, since the integrals of $F_L$ and $F_H$ are feedback controlled to coincide with those of $R_L$ and $R_H$, the integral of $\Delta(R_H - R_L)/2\gamma$, the integral of current and equals to the battery charge, can be correctly measured as the integral of $\Delta(F_H - F_L)/2\gamma$. The magnetic field change faster than CR cannot be tracked by $\Delta(F_H - F_L)/2\gamma$ and remains in $P_Q$ and $P_N$.

The two independent feedback controls for sensors A and B allowed for differences in their quality or size. However, the parallelism of the magnetic detection axes (i.e., the NV-axes) of sensors A and B is an important parameter for realizing high sensitivity of the gradiometer.

To discuss the Common Mode Rejection Ratio (CMRR) of the gradiometer, the tilt angle $\theta$ between the NV-axes of the sensors A and B is defined as shown in Figure 2d. The external magnetic noise field in-plane component of the NV axes is also defined as $B_\parallel$ and $B_\perp$ which are parallel and perpendicular to the bisector of two NV-axes as shown in the same figure. The magnetic field sensed by sensors A and B, $B_A$ and $B_B$ is then:

$$B_A = B_{||} \cos\frac{\theta}{2} + B_\perp \sin\frac{\theta}{2} \tag{1}$$

$$B_B = B_{||} \cos\frac{\theta}{2} - B_\perp \sin\frac{\theta}{2} \tag{2}$$

CMRR is then

$$\text{CMRR} = \frac{B_A - B_B}{B_A + B_B} = \frac{B_\perp \sin\frac{\theta}{2}}{B_{||} \cos\frac{\theta}{2}} \tag{3}$$

We assume that $B_\parallel$ and $B_\perp$ are statistically even because they are generally random noise. Then CMRR becomes:

$$\text{CMRR} = \tan\frac{\theta}{2} \tag{4}$$

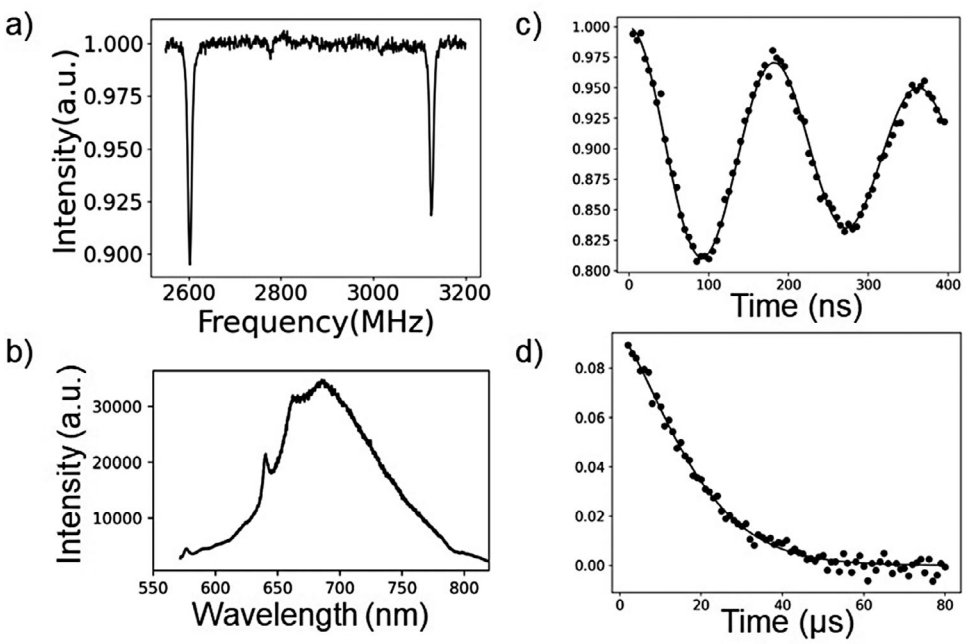


**Figure 3.** Fundamental physical properties of the heteroepitaxial CVD diamond sensor were measured with a confocal microscope. a) CW-ODMR spectrum, b) PL spectrum, c) Rabi oscillation, d) Hahn echo decay.

This relationship between CMRR and $\theta$ is shown in Figure 2e. To achieve a CMRR of 0.01 (−40 dB), the tilt must be aligned to 1° or less. For HPHT diamond, such precise alignment is not very difficult because the cleavage realizes the exact (111) surface. In contrast, CVD diamonds are often accompanied by misorientation, which ranges from a few to sometimes ≈10°.[33] The following procedure was used for the tilt correction to attain the desired CMRR.

The busbar was placed at the center of the 3-axis Helmholtz coil. A static magnetic field of ≈2 mT was applied along the Z axis. Subsequently, an AC magnetic field was applied along the X or Y axis. The AC magnetic field was perceived by the sensors to the extent that the NV-axes were tilted with respect to the Z axis. The tilt angle between the sensor surface and the busbar was adjusted with the screws shown in Figure 2f so that the detected AC magnetic field was minimized.

## 4. Results and Discussions

Figure 3 shows the results of confocal microscopy to evaluate the fundamental physical properties. A diode-pumped solid-state laser with a wavelength of 532 nm was used as the excitation laser. The diamond sample was irradiated with laser light using an oil-immersion objective lens. Fluorescence from the NV center was detected with an avalanche photodiode through a pinhole ($\varphi$30 μm) and a long-path filter (cut-off: 633 nm). The in-plane spatial resolution was ≈500 nm. Single NV counts excited by a 0.6 mW of laser were $1.6 \times 10^5$ cps. Figure 3a shows the continuous wave optically detected magnetic resonance (CW-ODMR) spectrum with an applied magnetic field of ≈9 mT along the (111) direction. Two resonance peaks from perfectly aligned NV centers were observed in this spectrum. Figure 3b shows the photoluminescence (PL) spectrum. A typical PL spectrum from the negatively charged NV ($NV^-$) centers was observed. Figure 3c shows the Rabi oscillations measured using the pulsed ODMR method. The Rabi contrast and Rabi periods were evaluated as 23% and 180 ns, respectively. Figure 3d shows the Hahn echo decay measured with the alternating Hahn echo sequence as follows: After initialization with the laser pulses, the spin states were read out by the laser pulses after irradiation with microwave (MW) pulses of $\pi_x/2$-$\pi_x$-$\pi_x/2$ and $\pi_x/2$-$\pi_x$-$\pi_{-x}/2$. Between each MW pulse, there was an evolution time tau during which both the laser and MW were switched off. The duration of the $\pi/2$ and $\pi$ MW pulses were estimated to be 45 and 90 ns, respectively, based on the evaluated Rabi period. $\pi_x/2$ and $\pi_{-x}/2$ are MW pulses with a phase difference of 180°. The spin state was read out using a laser pulse after the MW pulse irradiation. The signals detected after the last $\pi_x/2$ and $\pi_{-x}/2$ MW pulse irradiation are labeled $I_1$ and $I_2$, respectively. To remove the noise component, the detected signals were normalized using the following equation and shown as the vertical axis in Figure 3d:

$$\text{Intensity} = \left(I_1 - I_2\right) / \left(I_1 + I_2\right) \tag{5}$$

The spin coherence time $T_2$ was estimated to be 20 μs based on the normalized Hahn echo decay. The substitutional nitrogen defect concentration was determined from $T_2$ as $1.4 \times 10^{18}$ $cm^{-3}$.[35]

**Figure 4** shows the fundamental performance of the diamonds as a fiber-top sensor installed in the sensor holder for busbar current measurement. The CW-ODMR spectrum is shown in Figure 4a. Compared with the spectrum in Figure 3a, which was measured with a confocal microscope, some peaks other than [111] were also observed. The reason for this is probably due to the fact that the fluorescence of the entire volume of the diamond

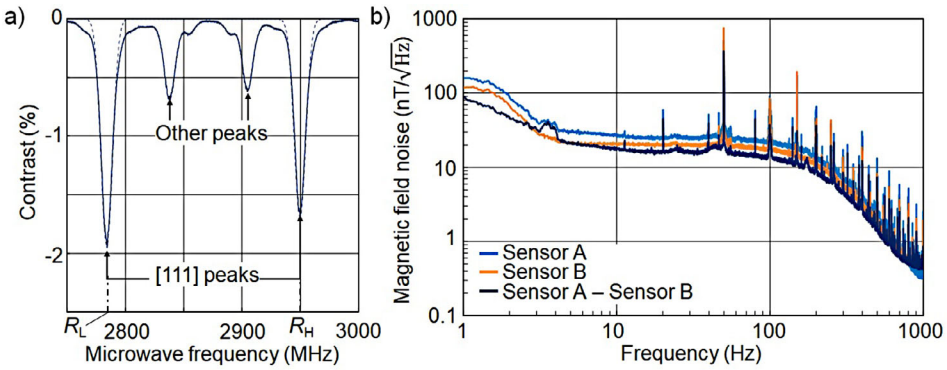


**Figure 4.** Fundamental performance of the heteroepitaxial (111) CVD diamond sensor glued onto the fiber-top and installed in the sensor holder for busbar current measurement. a) CW-ODMR spectrum showing NV-axes preferentially aligned to (111). The dashed line represents the Gaussian fit. b) FFT spectra of the magnetic field noise observed as $(P_Q - P_N)/2\gamma S$, where $P_Q$ and $P_N$ are the normal and quadrature two-phase outputs of the lock-in amplifier, $\gamma$ is the gyromagnetic ratio and $S$ is the rate of change (slope) of the derivative of the ODMR spectrum at the resonance frequency. The blue and orange lines represent independent sensors A and B, respectively, while the dark blue represents their difference as the gradiometer.

sensor including the peripheral edge or the substrate bottom where crystal growth could be irregular is collected in the fiber-top implementation. The $T_2^*$ value estimated from the Gaussian fit of the [111] peaks shown in Figure 4a was 0.05 µs. In Figure 4a, the photodiode current for contrast 0% was 0.9 µA at 60-mW 532-nm excitation light. From this value, the $NV^-$ concentration in the heteroepitaxial diamond can be estimated to be ≈0.05 ppm.

Figure 4b shows the FFT spectra of the magnetic field noise of sensors A and B observed as $(P_Q - P_N)/2\gamma S$, where $S$ is the rate of change (slope) of the derivative of the ODMR spectrum at the resonance frequency. The noise floor of the independent sensors A and B in the frequency range of 10–40 Hz were 25 and 21 nT/$\sqrt{\text{Hz}}$, respectively. The frequency peaks correspond to the utility frequency (i.e., 50 Hz) and its harmonics. In the case of the gradiometer, taking their difference, the noise floor was 17 nT/$\sqrt{\text{Hz}}$.

**Figure 5** shows the common mode noise rejection characteristics as the gradiometer in the laboratory noise environment. The Allan deviation of the magnetic field without the busbar current is shown in Figure 5a, where the magnetic field was evaluated as the sum of $\Delta(P_Q - P_N)/2\gamma S$ which is dominant at shorter time range than CR and $\Delta(F_H - F_L)/2\gamma$ which is dominant at longer time range.

The black dashed line at 0.3 µT corresponds to a busbar current of 10 mA.

Since the noise contains various external noise components, the slope is not a monotonic gradient of −0.5. In the short-time side of this figure, the internal system noise, including the excitation laser noise, is considered to be dominant, whereas on the long-time side, the external environmental noise is considered dominant. On the long-time side, the Allan deviations of independent sensors A and B exceed the 10 mA line, but that of A−B is certainly below the 10 mA line, indicating that 10 mA detection is possible without magnetic shielding in the accumulation time range between 10 ms and 100 s.

To confirm that a few mA can be detected in the time domain in a noisy environment, a current pulse train with an amplitude between 100 and 1 mA as shown in Figure 5b was applied as

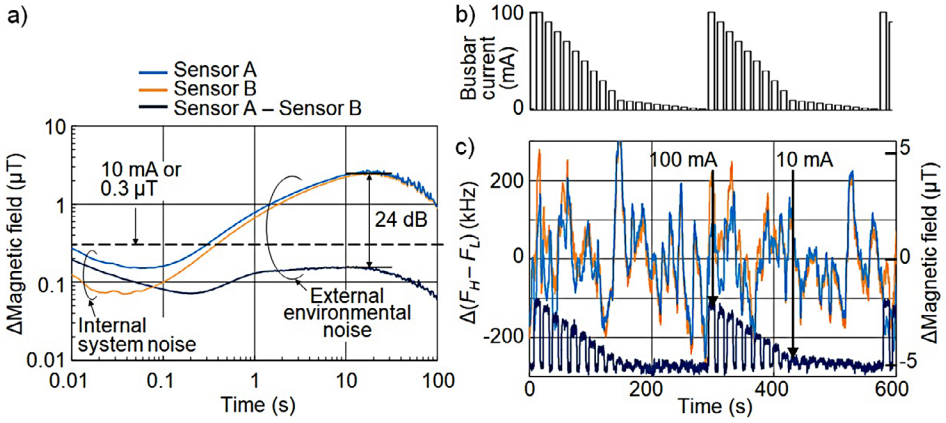


**Figure 5.** Common mode noise rejection characteristics of heteroepitaxial CVD diamond sensors as the gradiometer measured in the laboratory noise environment. a) Allan deviation of the magnetic field without the busbar current, where the magnetic field was evaluated as the sum of $\Delta(P_Q - P_N)/2\gamma S$ which is major at shorter time range than CR and $\Delta(F_H - F_L)/2\gamma$ which is major at longer time range. The blue and orange lines represent independent sensors A and B, respectively, while the dark blue represents their difference as the gradiometer. b) Busbar current from 100 to 1 mA for pulse measurement. c) Measured magnetic field in pulse measurement. Blue, orange, and dark blue lines are the same as in (a). A 10 mA pulse could be recognized.

the target signal to the busbar from an external current source (Keithley 2280S-32-6). Figure 5c shows the outputs of each heteroepitaxial sensor A and B, and their differences. The left vertical axis is shown as $\Delta(F_H - F_L)$ in kHz, and the right vertical axis is shown as $\Delta(F_H - F_L)/2\gamma$ in μT. Although the individual sensors could not even detect a 100 mA pulse, the difference A-B could detect 10 mA.

The Allan deviations of the magnetic field noise shown in Figure 5a and the noise waveform in Figure 5c are discussed. The Allan deviation shows the average value over the accumulation time, whereas the pulse waveform in Figure 5c contains instantaneous changes. Under a noise field in the laboratory, the instantaneous noise can reach 0.3 μT, although the average value is less than 0.3 μT, corresponding to a differential output of 10 mA. This is probably due to the fact that the fluorescence photocurrent was as low as 0.9 μA, so the differential output was buried by the system noise. To keep the instantaneous noise below 0.3 μT, the improvement of the photocurrent through the electron beam irradiation into the heteroepitaxial diamonds or the improvement of the fluorescence collection efficiency of the fiber-top sensor[36–39] should be effective. The improvement of the relatively short $T_2^*$, which was 0.05 μs in this study, probably due to the strain distribution in the diamond, should also improve the shot noise. The double-quantum protocol[40] would be effective for this purpose.

## 5. Conclusion and Summary

A platform for heteroepitaxial (111) diamond quantum sensors with preferentially aligned NV centers on large substrates was developed, which could facilitate their implementation as EV battery monitors. The diamonds were synthesized on a non-diamond substrate and exhibited high uniformity and crystallinity with a (111) surface orientation, and the NV axis was preferentially aligned to the surface-normal direction [111]. Two diamond sensors were placed on both sides of the busbar through which the EV battery current flowed to remove the external magnetic field noise as common mode noise using the gradiometer effect.

The misorientation between the substrate surface and the (111) plane associated with the CVD process could degrade the common mode rejection ratio. The tilt angle between the (111) planes of the two sensors in the gradiometer was minimized by mechanically adjusting the screws in the sensor holder. The Allan deviation of the gradiometer was below 0.3 μT, which corresponded to the 10 mA busbar current, in the time range of 0.01–100 s under the external magnetic field of a few micro-teslas without magnetic shielding.

To ensure the detection of 10 mA in the real noise environment of automobiles with tens of micro-teslas, further efforts to increase the photocurrent are expected, such as increasing the NV density by electron beam irradiation into the diamond sensors and improving the fluorescence collection efficiency of the sensor head. Extending the $T_2^*$ of the diamond sensors using quantum protocols would also mitigate the effects of noise.

## Acknowledgements

This work was supported by the MEXT Quantum Leap Flagship Program (MEXT Q-LEAP) Grant Number JPMXS0118067395.

## Conflict of Interest

The authors declare no conflict of interest

## Data Availability Statement

The data that support the findings of this study are available from the corresponding author upon reasonable request.

## Keywords

diamond, current sensor, EV battery, heteroepitaxial CVD, NV center

Received: August 17, 2024
Revised: December 9, 2024
Published online: January 18, 2025

[1] F. Jelezko, T. Gaebel, I. Popa, A. Gruber, J. Wrachtrup, *Phys. Rev. Lett.* **2004**, *92*, 076401.
[2] J. Taylor, P. Cappellaro, L. Childress, L. Jiang, D. Budker, P. R. Hemmer, A. Yacoby, R. Walsworth, M. Lukin, *Nat. Phys.* **2004**, *4*, 810.
[3] J. Maze, P. Stanwix, J. Hodges, S. Hong, J. Taylor, P. Cappellaro, L. Jiang, M. Dutt, E. Togan, A. Zibrov, A. Yacoby, R. Walsworth, M. Lukin, *Nature* **2008**, *455*, 644.
[4] G. Balasubramanian, I. Chan, R. Kolesov, M. Al-Hmoud, J. Tisler, C. Shin, C. Kim, A. Wojcik, P. Hemmer, A. Krueger, T. Hanke, A. Leitenstorfer, R. Bratschitsch, F. Jelezko, J. Wrachtrup, *Nature* **2008**, *455*, 648.
[5] V. Acosta, E. Bauch, M. Ledbetter, C. Santori, K. Fu, P. Barclay, R. Beausoleil, H. Linget, J. Roch, F. Treussart, S. Chemerisov, W. Gawlik, D. Budker, *Phys. Rev. B.* **2009**, *80*, 115202.
[6] Y. Hatano, J. Shin, J. Tanigawa, Y. Shigenobu, A. Nakazono, T. Sekiguchi, S. Onoda, T. Ohshima, K. Arai, T. Iwasaki, M. Hatano, *Sci. Rep.* **2022**, *12*, 13991.
[7] Y. Hatano, J. Tanigawa, A. Nakazono, T. Sekiguchi, S. Onoda, T. Ohshima, T. Iwasaki, M. Hatano, *Phil. Trans. R. Soc. A.* **2023**, *382*, 20220312.
[8] K. Kubota, Y. Hatano, Y. Kainuma, J. Shin, D. Nishitani, C. Shinei, T. Taniguchi, T. Teraji, S. Onoda, T. Ohshima, T. Iwasaki, M. Hatano, *Diamond Relat. Mater.* **2023**, *135*, 109853.
[9] J. Yaita, T. Iwasaki, M. Natal, S. E. Saddow, M. Hatano, *Jpn. J. Appl. Phys.* **2015**, *54*, 04DH13.
[10] J. Yaita, M. Natal, S. E. Saddow, M. Hatano, T. Iwasaki, *Appl. Phys. Express.* **2017**, *10*, 045502.
[11] T. Suto, J. Yaita, T. Iwasaki, M. Hatano, *Appl. Phys. Lett.* **2017**, *110*, 062102.
[12] H. Aida, S. Kim, K. Ikejiri, D. Fujii, Y. Kawamata, K. Koyama, H. Kodama, A. Sawabe, *Diamond Relat. Mater.* **2017**, *75*, 34.
[13] K. Ichikawa, H. Kodama, K. Suzuki, A. Sawabe, *Diamond Relat. Mater.* **2017**, *72*, 114.
[14] E. Moore, J. Jarrell, L. Cao, *Heliyon* **2017**, *3*, e00404.
[15] J. Yaita, M. N. T. Suto, S. E. Saddow, M. Hatano, T. Iwasaki, *Diamond Relat. Mater.* **2018**, *88*, 158.
[16] J. Yaita, T. Tsuji, M. Hatano, T. Iwasaki, *Appl. Phys. Express* **2018**, *11*, 045501.
[17] G. Shu, B. Dai, V. Ralchenko, A. Bolshakov, A. Khomich, E. Ashkinazi, V. Yurov, K. Yao, K. Liu, J. Zhao, J. Han, J. Zhu, *J. Cryst. Growth* **2018**, *486*, 104.
[18] B. Gallheber, M. Fischer, M. Mayr, J. Straub, M. Schreck, *J. Appl. Phys.* **2018**, *123*, 225302.

[19] M. Frank, O. Sabine, G. Andreas, R. Eduard, C. Eva-Regine, F. Alexander, W. Marco, G. Lukas, B. Frank, *Thin Solid Films* **2018**, *650*, 65.
[20] M. Schreck, S. Gsell, M. Fisher, B. Gallheber, M. Mayr, M. Träger, M. Kiš, *Symp. Latsis Diamond Photonics* **2019**, 77.
[21] R. Nelz, J. Görlitz, D. Herrmann, A. Slablab, M. Challier, M. Radtke, M. Fischer, S. Gsell, M. Schreck, C. Becher, E. Neu, *APL Mater.* **2019**, *7*, 011108.
[22] S. Zhang, C. Zhao, Y. Zhu, Y. Fang, S. Li, M. He, Y. Hang, *Mater. Chem. Phys.* **2021**, *273*, 125152.
[23] S.-W. Kim, K. Koyama, M. Kasu, *New Diamond* **2021**, *37*, 30.
[24] S.-W. Kim, M. Kasu, *CS MANTECH Conference* **2022**, 19.
[25] U. Choi, H. Shin, T. Kwak, S. Kim, O. Nam, *Diamond Relat. Mater.* **2022**, *121*, 108770.
[26] W. Wang, K. Liu, S. Yang, V. Ralchenko, J. Han, B. Dai, *Vacuum* **2022**, *204*, 111374.
[27] P. Qu, P. Jin, G. Zhou, Z. Wang, Z. Wang, *J. Semicond.* **2024**, *45*, 090501.
[28] M. Kasu, R. Takaya, S.-W. Kim, *Diamond Relat. Mater.* **2022**, *126*, 109086.
[29] T. Fukui, Y. Doi, T. Miyazaki, Y. Miyamoto, H. Kato, T. Matsumoto, T. Makino, S. Yamasaki, R. Morimoto, N. Tokuda, M. Hatano, Y. Sakagawa, H. Morishita, T. Tashima, S. Miwa, Y. Suzuki, N. Mizuochi, *Appl. Phys. Express* **2014**, *7*, 055201.
[30] J. Michl, T. Teraji, S. Zaiser, I. Jakobi, G. Waldherr, F. Dolde, P. Neumann, M. Doherty, N. Manson, J. Isoya, J. Wrachtrup, *Appl. Phys. Lett.* **2014**, *104*, 102407.
[31] M. Lesik, J. Tetienne, A. Tallaire, J. Achard, V. Mille, A. Gicquel, J. Roch, V. Jacques, *Appl. Phys. Lett.* **2014**, *104*, 113107.
[32] H. Ozawa, K. Tahara, H. Ishiwata, M. Hatano, T. Iwasaki, *Appl. Phys. Express* **2017**, *10*, 045501.
[33] T. Tsuji, T. Sekiguchi, T. Iwasaki, M. Hatano, *Adv. Quantum Technol.* **2023**, *7*, 2300194.
[34] Y. Hatano, J. Shin, D. Nishitani, H. Iwatsuka, Y. Masuyama, H. Sugiyama, M. Ishii, S. Onoda, T. Ohshima, K. Arai, T. Iwasaki, M. Hatano, *Appl. Phys. Lett.* **2021**, *118*, 034001.
[35] E. Bauch, S. Singh, J. Lee, C. A. Hart, J. M. Schloss, M. J. Turner, J. F. Barry, L. M. Pham, N. Bar-Gill, S. F. Yelin, R. L. Walsworth, *Phys. Rev. B* **2020**, *102*, 134210.
[36] R. Patel, L. Zhou, A. Frangeskou, G. Stimpson, B. Breeze, A. Nikitin, M. Dale, E. Nichols, W. Thornley, B. Green, M. Newton, A. Edmonds, M. Markham, D. Twitchen, G. Morley, *Phys. Rev. Appl.* **2020**, *14*, 044058.
[37] R. Katsumi, T. Hizawa, A. Kuwahata, S. Naruse, Y. Hatano, T. Iwasaki, M. Hatano, F. Jelezko, S. Onoda, T. Ohshima, M. Sekino, T. Yatsui, *Appl. Phys. Lett.* **2022**, *121*, 161103.
[38] S. Zhang, H. Lin, Y. Dong, B. Du, X. Gao, C. Yu, Z. Feng, X. Chen, G. Guo, F. Sun, *Photonics Res.* **2022**, *10*, 2191.
[39] S. Graham, A. Rahman, L. Munn, R. Patel, A. Newman, C. Stephen, G. Colston, A. Nikitin, A. Edmonds, D. Twitchen, M. Markham, G. Morley, *Phys. Rev. Appl.* **2023**, *19*, 044042.
[40] I. Fujisaki, Y. Araki, Y. Hatano, T. Sekiguchi, H. Kato, S. Onoda, T. Ohshima, T. Shibata, T. Iwasaki, M. Hatano, *Phys. Status Solidi A* **2024**, *221*, 2300333.